Supporting Information

Superhydrophobic gradient wrinkle strain sensor with ultra-high sensitivity and broad strain range for motion monitoring

Zhenming Chu [a], Weicheng Jiao [a, *], Yifan Huang [a], Yongting Zheng [a], Rongguo Wang [a], and Xiaodong He [a, b]

[a] *National Key Laboratory of Science and Technology for National Defence on Advanced Composites in Special Environments, Harbin Institute of Technology, Harbin, 150080, China*

[b] *Shenzhen STRONG Advanced Materials Research Institute Co., Ltd, Shenzhen, 518063, China*

Corresponding Authors: *E-mail: xiaojiao458@163.com

Preparation section:

Preparation of PDMS/Au/rGO plane strain sensor. The rGO film was transferred to the VHB substrate and put in the ion sputtering apparatus for plating a layer of gold to obtain the Au/rGO gradient wrinkle film. Thereafter, the PDMS/Au/rGO strain sensor was obtained by spinning a layer of PDMS coating solution on the spin coater at 2000 r/min for 10 s and drying at 60 ℃ for 4 h.

Preparation of rGO/PDMS wrinkle strain sensor. The resulting rGO film was transferred to the biaxial pre-stretched (pre-strain of 300%) VHB substrate. Releasing the substrate along the symmetrical direction to the original size to obtained rGO wrinkle film. The rGO/PDMS wrinkle strain sensor was obtained by spinning the PDMS coating solution with the same method as above.

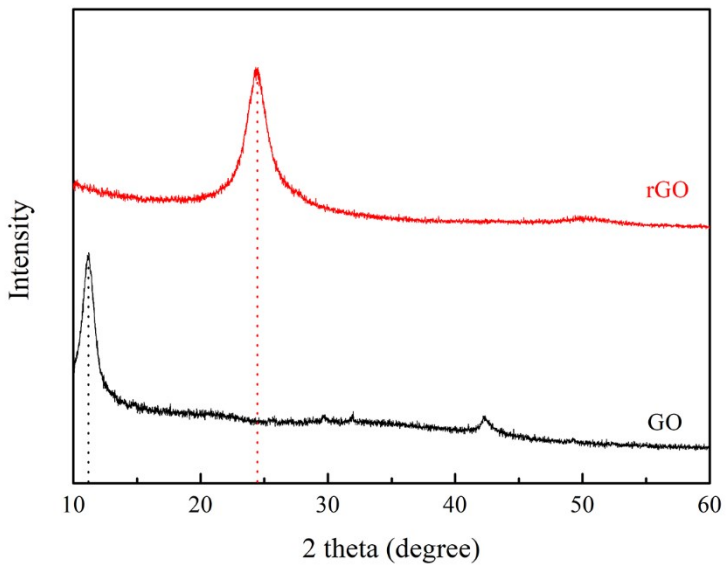

Fig. S1. XRD pattern of GO and rGO.

The rGO was identified by the XRD pattern, as shown in Fig. S1. After treating the GO film with HI, the main peak changed from the 11.27° to 24.38° with interplanar

distance reduced from 0.78 nm to 0.36 nm, which indicated that the oxygen-containing functional groups on the GO surface were reduced to obtained rGO.[1, 2]

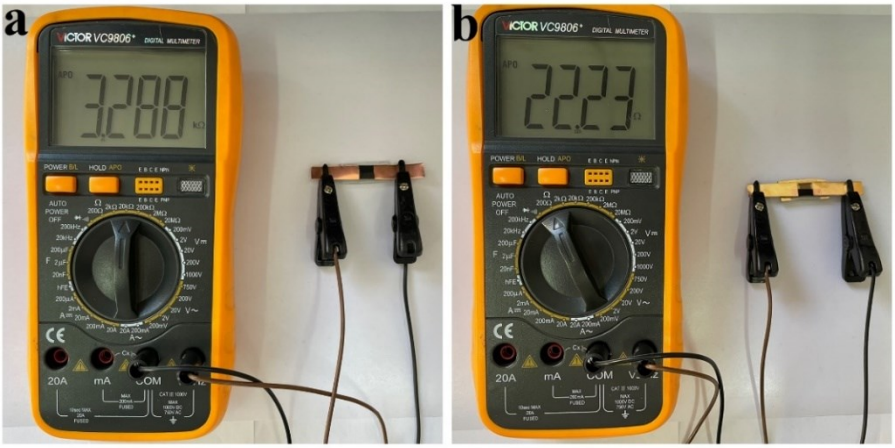

Fig. S2. (a) The resistance value of the strain sensor without gold film in Zone-Ⅱ. (b) The resistance value of the strain sensor with gold film in Zone-Ⅱ.

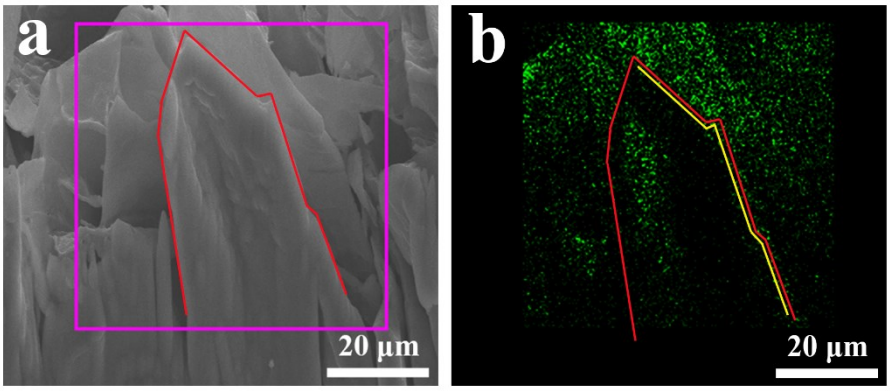

Fig. S3. (a) Cross-sectional SEM morphology image of the strain sensor. (b) EDS mapping images of Si.

The thickness of PDMS on the PRGW surface was estimated by silicon EDS scanning of Si on the cross section. The boundary of the Si element distribution in Fig. S3 (b) is marked, and it can be obtained that the thickness of PDMS is about 345 nm.

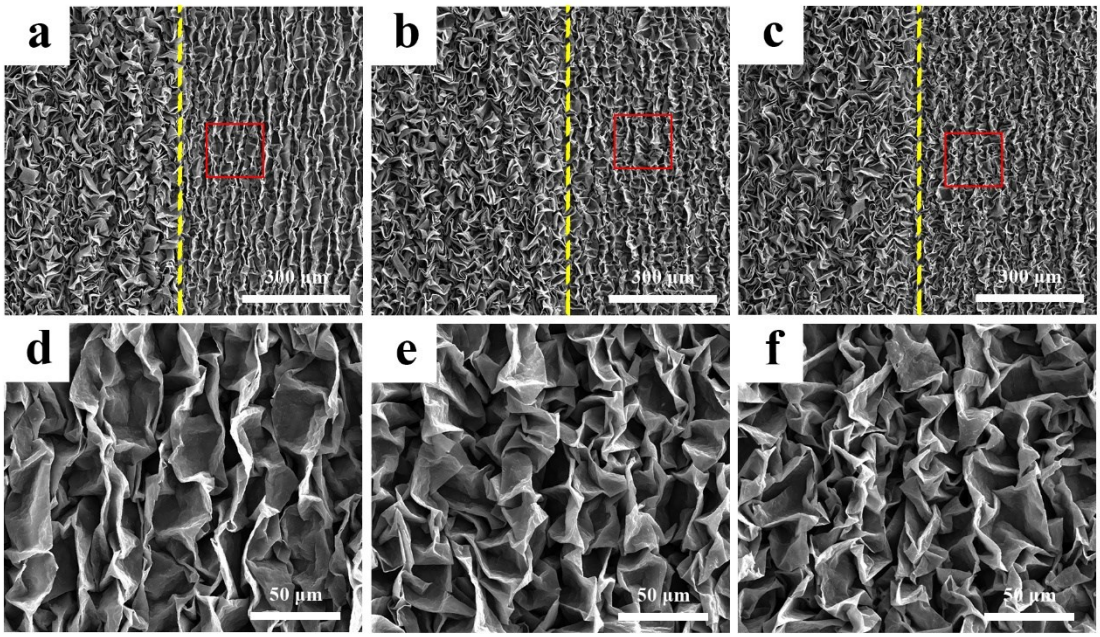

Fig. S4. (a-c) Ordinal SEM images of strain sensors with pre-strain along the Y-axis in Zone-Ⅱ are 30%, 60%, and 90%, respectively. (d), (e), (f) Highly magnified SEM images of Zone-Ⅱ of (a), (b), and (c), respectively.

As shown in Fig. S4a- S4c, the wrinkle degrees of Zone-Ⅰ of the three strain sensors were the same with gradient structure; while the wrinkle degree of Zone-Ⅱ gradually increased with the increase of tensile strain along the Y-axis during the preparation process.

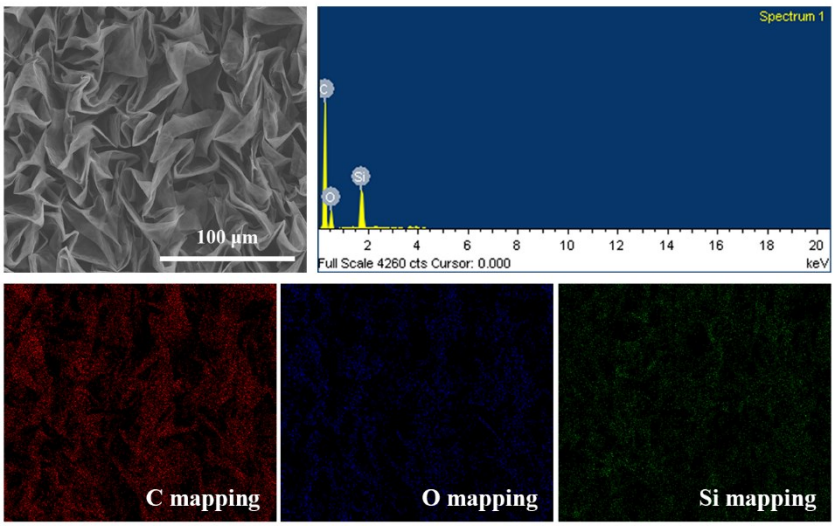

Fig. S5. EDS mapping images of C, O, Si in the Zone-Ⅰ of the PRGW strain sensor.

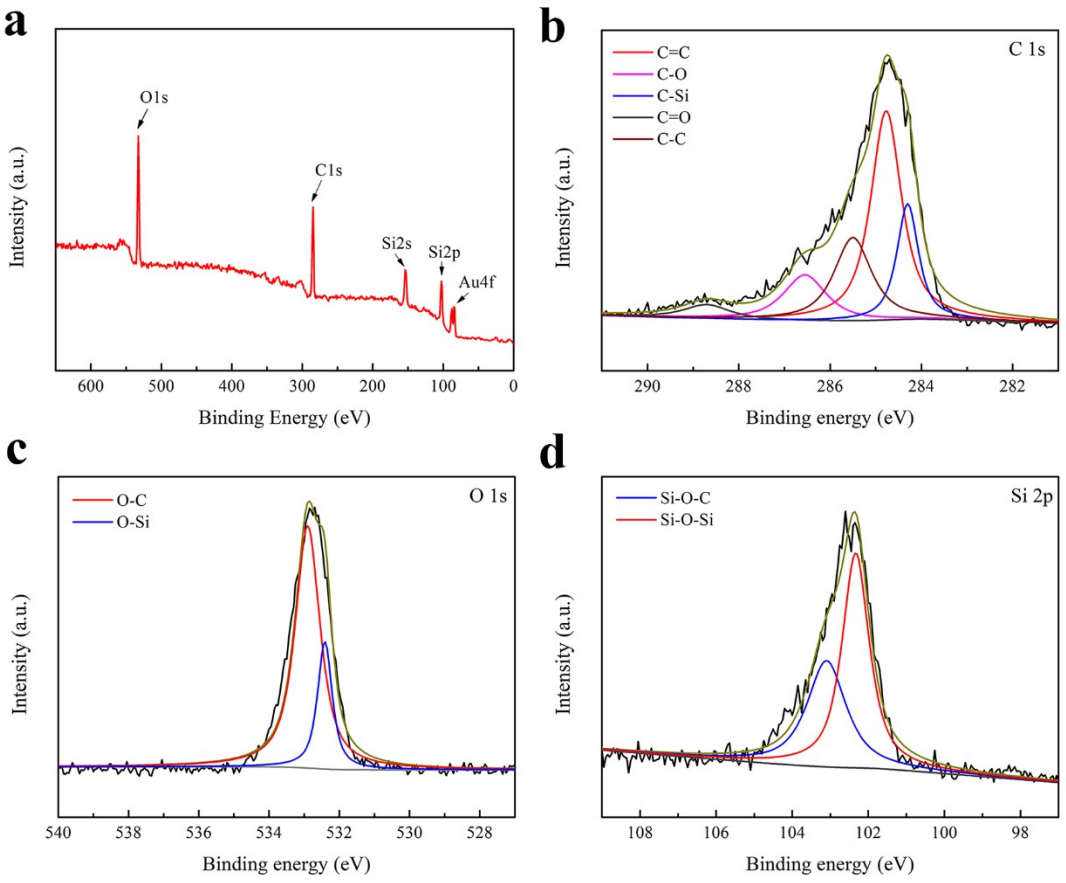

Fig. S6. (a) The XPS full spectra of the PRGW strain sensor, (b) C 1s area of the PRGW (c) and O 1s area of the PRGW, (d) Si 2p area of the PRGW.

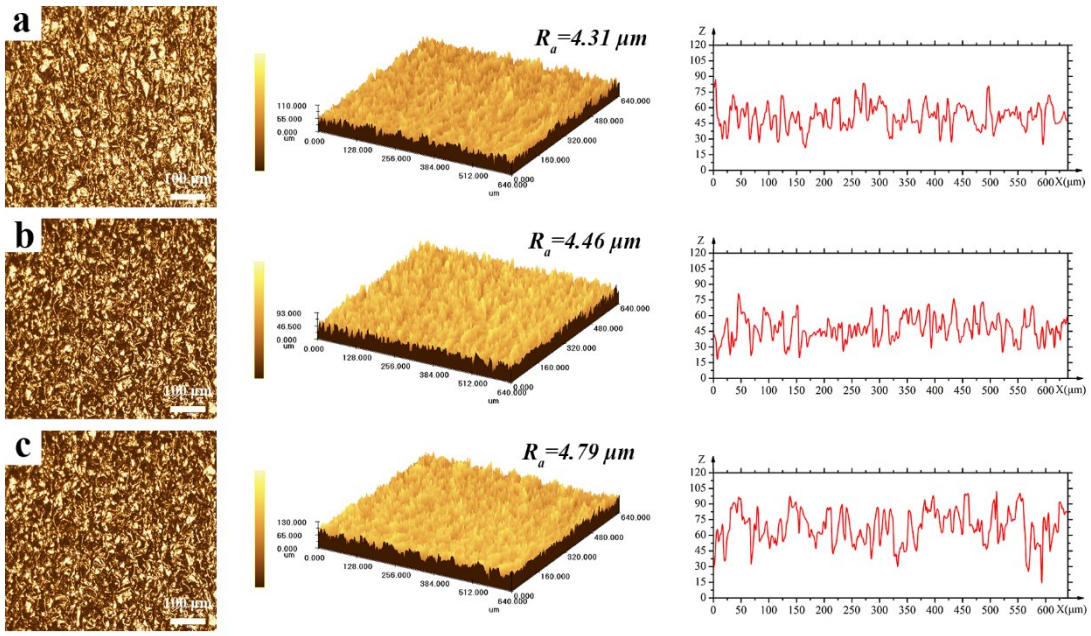

Fig. S7. (a) LSCM profile and R_a of Zone-Ⅱ of the strain sensor with a pre-strain of 30% along the Y-axis. (b) LSCM profile and R_a of Zone-Ⅱ of the strain sensor with a pre-strain of 60% along the Y-axis. (c) LSCM profile and R_a of Zone-Ⅱ of the strain sensor with a pre-strain of 90% along the Y-axis.

As shown in Fig. S7, the roughness of the wrinkle increased from 4.31 μm to 4.79 μm as the pre-strain increases from 30% to 90% during the preparation process. The height variation diagram along the Z-axis exhibited that the convex height of the wrinkle will also increase with the increase of pre-strain.

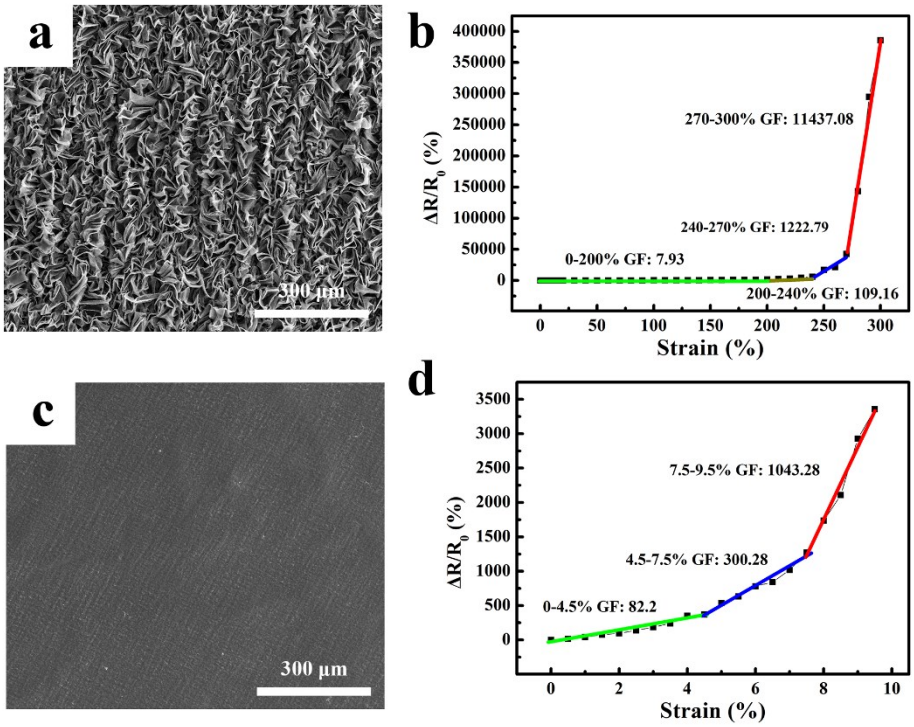

Fig. S8. (a) SEM of the PDMS/rGO wrinkle strain sensor. (b) The resistance of the wrinkle strain sensor varies with the strain. (c) SEM of the PDMS/Au/rGO plane strain sensor. (d) The resistance of the plane strain sensor varies with the strain.

Fig. S9. (a) The resistance value of the rGO gradient wrinkled strain sensor. (b) The resistance value of the PRGW strain sensor.

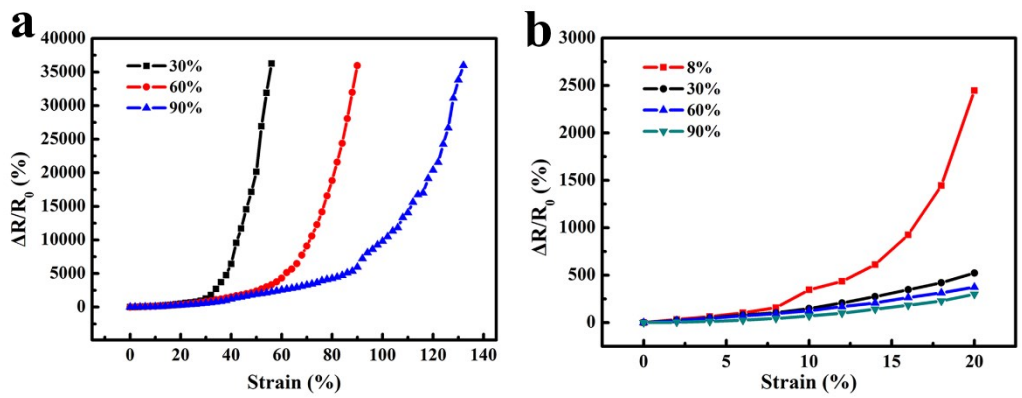

Fig. S10. (a) The resistance of different strain sensors varies with the strain. (b) the strain sensing performance of different strain sensors in the small strain range.

As shown in Fig. S10a, the three curves represent the strain sensing performance of the sensor obtained in the preparation process when the pre-strain along the Y-axis is 30%, 60%, and 90%, respectively. During the stretching process, the mutant values of the resistance (i.e. the high sensitivity position) appeared at the strain position of 30%, 60%, and 90%, which mainly due to cracks in the wrinkles of Zone-Ⅱ at that position. Therefore, the position of the sensor's high sensitivity can be controlled by adjusting the pre-strain in the preparation process. What's more, it can be seen from Fig. S10b that with the decrease of pre-strain during preparation, the sensitivity of the low strain range increased gradually even before cracks appear. This is mainly since under the same condition of tensile strain, the morphology of the sensor changes relatively great with the reduction of wrinkle degree, leading to a great change in the conductive path.

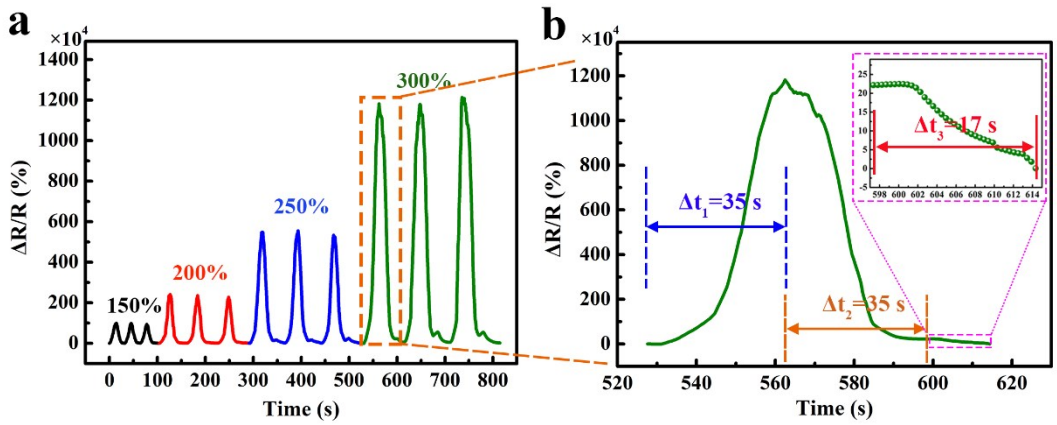

Fig. S11. (a) Cycle test under different large strains (150%, 200%, 250%, and 300%). (b) Variation of strain with time when strain varies between 0% and 300%.

The strain sensor is fixed to the guide rail module, and the degree and rate of stretching and shrinking are controlled by a stepping motor. It can be seen from the figure that the repeatability is good at various strains, which proves that the sensor still maintains good stability in a large strain range.

The response and recovery time of the sensor were analyzed at the same stretching and retracting rates, as shown in Fig. S11(b). In the stretching phase, the strain sensor moves with the guide rail module to a strain of 300%, and the required time is Δt_1=35 s; in the shrinking phase, the guide rail module returns to the starting point, and the required time is Δt_2=35 s. However, the ΔR/R of the strain sensor returns to the initial value and it takes 17 s to be used again (as shown in the inset). This is mainly due to the fact that the VHB basement membrane cannot be restored to its original appearance in real time after stretching at a large strain. Although the strain sensor has hysteretic behavior, its overall recovery degree is good.

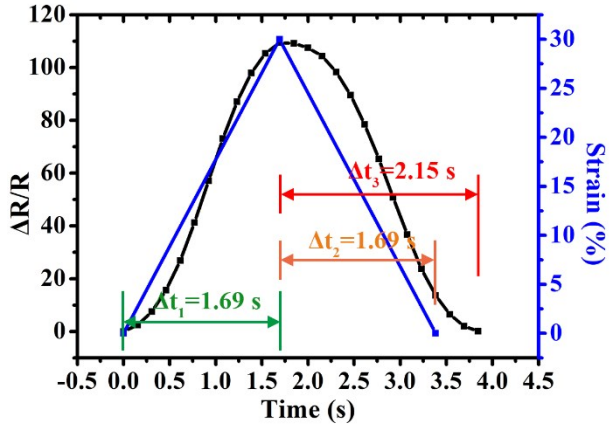

Fig. S12. Changes in ΔR/R and strain with time when the strain changes from 0% to 30%

As shown in Fig. S12, the time the sensor takes for the strain to increase from 0% to 30% is 1.69s, which is the same as the time it takes for the ΔR/R of the strain sensor to increase to the maximum, which proves that the stretching process can respond in real time. In the retraction process, the stretching length of the sensor is restored to the original size in 1.69s, while the recovery of the resistance signal is 2.15s, showing a delay of 0.46s, which is manily because the hysteresis of the VHB substrate during retraction.

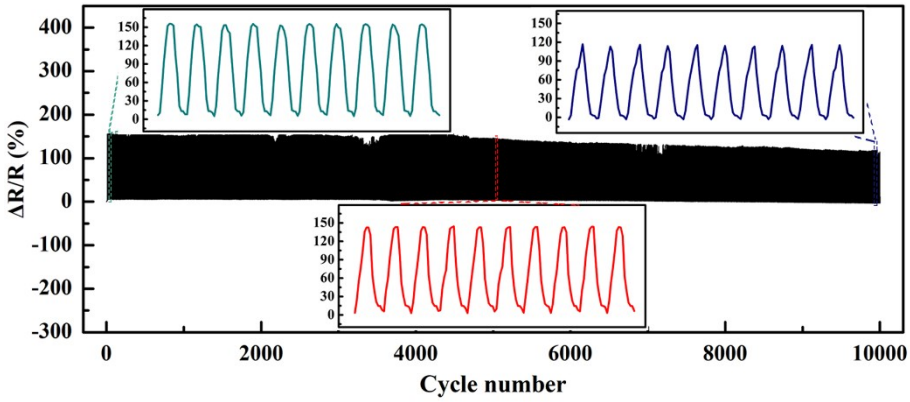

Fig. S13. Bending cycle test of the PRGW strain sensor.

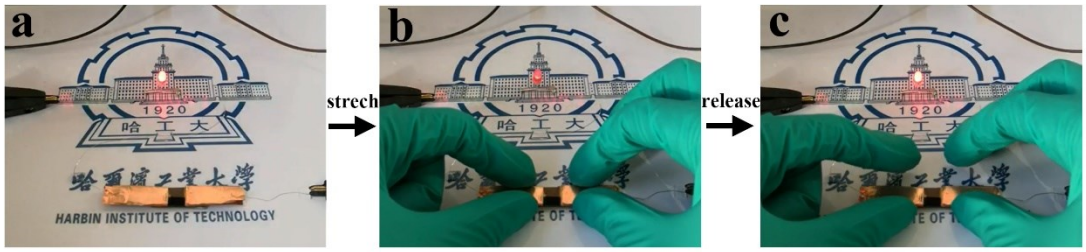

Fig. S14. Strain sensors are used to control the brightness of a LED lamp.

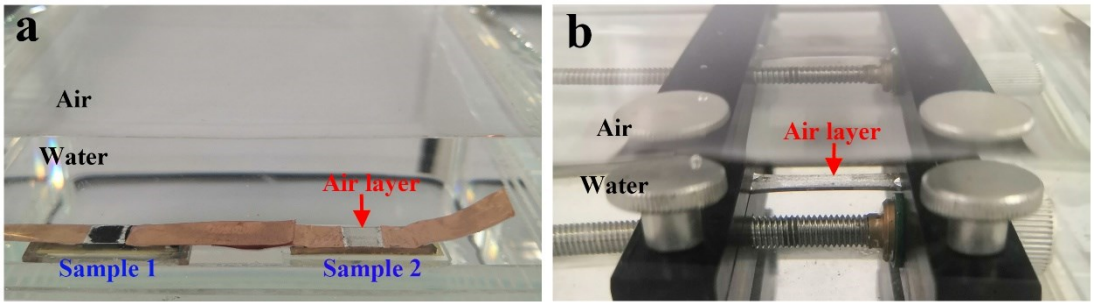

Fig. S15. (a) The strain sensors are immersed in water. (b) The PRGW strain sensor with a strain of 300% is immersed in water.

As shown in Fig. S15, sample 1 and sample 2 are rGO wrinkle and PRGW, respectively. Since there is no PDMS layer on the surface of sample 1, it presented a normal color underwater, which proved that the surface is completely wetted by water. Due to the super-hydrophobic property of sample 2, there was an air layer between the water and the sample surface, which made the light reflect at the water/air interface and presented a bright color.[3] Besides, when the strain of PRGW was 300%, it still had bright color underwater, proved that the air layer still existed. Therefore, the sensor still has good super-hydrophobic performance in large strain and can be applied to underwater sensing.

Strain sensors	Max sensing range	Gauge factor	Detection limit	Stability (Cycle tested)	Super-hydrophobicity	Year	Reference
MXene/CNT	130%	64.6 (0%–30%) 772.6 (40%–70%)	0.1%	5,000 cycles	N/A	2018	[30]
CNTs	150%	161 (0%–2%) 9.8 (10%–40%) 0.58 (15%–150%)	/	20,000 cycles	N/A	2015	[49]
Overlapped Carbon Nanotubes	145%	256 (0%–80%) 3250 (80%–125%) 42,300 (125%–145%)	＜1%	1,000 cycles	N/A	2019	[27]
Rubber band/AgNPs/PDMS	54.2%	36.7 (0%–32%) 264.9 (32.1%–47.9%) 1153.0 (48%–54.2%)	1%	2,000 cycles	Yes	2019	[40]
SEBS/AgNP	60%	66 (0%–51%) 1075 (53%–60%)	0.5%	1,000 cycles	Yes	2019	[41]
TPU/CNTs/PDMS nanofiber	100%	0.194 (0%–16%) 0.0714 (16%–50%) 0.339 (50%–100%)	/	700 cycles	Yes	2019	[34]
multi-walled carbon nanotubes/graphene	170%	49 (0%–100%) 177 (100%–160%) 2059 (160%–170%)	/	1,000 cycles	Yes	2020	[37]
Braided Graphene Belts	55.55%	175.16 (0%–34.91%) 1225.8 (35.9–49.7%) 13,278 (50.6–55.6%)	0.01%	6,000 cycles	N/A	2020	[50]
Graphene-PDMS/rGO	350%	18.5 (0%–80%) 448.5 (80%–200%) 6673 (200%–300%) 88,443 (300%–350%)	/	5,000 cycles	N/A	2019	[51]
Graphene nanocrystallite carbon film	15%	87 (0%–4%) 1071 (4%–15%)	/	150 cycles	N/A	2019	[52]
MXene/PANIF strain sensor	80%	97.6 (0%–10%) 563.6 (10%–40%) 2369.1 (40%–80%)	0.15%	2,500 cycles	N/A	2020	[53]
Graphene/Po							

lymer Composite							
PDA/rGO/TPU fibrous mats	150%	23.15 (0%–60%) 184.96 (60%–100%) 6583 (＞140%)	/	9,000 cycles	N/A	2020	[54]
carbon nanotube/SiO_2 nanoparticle network	80%	42 (0%–10%) 135 (10%–21%) 236 (22%–37%) 525 (37%–46%) 1766 (47%–57%)	0.1%	1200 cycles	Yes	2019	[55]
MXene	83%	2209.1 (60%–77%) 8767.4 (77%–83%)	/	5000 cycles	N/A	2018	[56]
CNT/TPU fibrous mat	300%	428.5 (＜100%) 9268.8 (100%–220%) 83982.8 (220%–300%)	0.5%	10000 cycles	N/A	2019	[57]
3D Porous Reduced Graphene Oxide Fiber Fabrics	70%	1668.48 (66.0%)	/	1200 cycles	N/A	2019	[58]
PDMS/rGO gradient wrinkle film	300%	9156.3 (20%–170%) 55785.8 (170%–270%) 167665.6 (270%–300%)	0.1%	10000 cycles	Yes		This work

Supplementary Information Reference:

1 S. Park, J. An, J. R. Potts, A. Velamakanni, S. Murali and R. S. Ruoff, *carbon*, 2011, **49**, 3019-3023.

2 G. Rajitha and R. K. Dash, *Sensors and Actuators A: Physical*, 2018, **277**, 26-34.

3 Y. Wang, J. Xue, Q. Wang, Q. Chen and J. Ding, *ACS applied materials & interfaces*, 2013, **5**, 3370-3381.